Nanoscale Advances

ROYAL SOCIETY OF CHEMISTRY

PAPER

View Article Online
View Journal | View Issue

Cite this: *Nanoscale Adv.*, 2025, **7**, 5300

Molybdenum carbide supported metal–organic framework-derived Ni, Co phosphosulphide heterostructures as efficient OER and HER catalysts†

Muhammad Ahsan Naseeb, Maida Murtaza, Komal Farooq, Waqas Ali Shah * and Amir Waseem *

Molybdenum carbide (Mo_xC) has gained attention for water splitting due to its electronic structure resembling to Pt and have high electrochemical performance. We designed porous nanostructured phosphorus/sulfur co-doped Ni, Co phosphosulphide and molybdenum carbide heterostructures Mo_xC(Mo_2C–MoC) through confined carburization within a metal–organic framework (MOF) matrix combined with a phosphosulfurization strategy. Starting from a carbon source consisting of NiCo–MOF incorporating molybdenum trioxide, we prepared MOF-derived NiCo–Mo_xC nanorods *via* carbonization, which exhibited decent electrocatalytic performance for the hydrogen evolution reaction (HER) by electrochemical water splitting. The NiCo–Mo_xC showed low overpotentials of 153 mV and 157 mV *vs.* RHE at a current density of 10 mA cm^{-2} in 0.5 M H_2SO_4 and 1 M KOH, respectively. Phosphosulfurization of NiCo–Mo_xC, performed under controlled conditions, resulted in the formation of NiPS–CoPS–Mo_xC, which demonstrated superior HER performance than the precursor NiCo–Mo_xC with overpotentials of 75.2 mV and 86.6 mV in 0.5 M H_2SO_4 and 1 M KOH, respectively and an overpotential of 184.5 mV at 10 mA cm^{-2} for the oxygen evolution reaction (OER). The durability of the NCMCSP-based electrolyzer for the overall water splitting was evaluated by measuring the voltage over time at a constant current density of 20 mA cm^{-2} for 12 h.

Received 24th May 2025
Accepted 5th July 2025

DOI: 10.1039/d5na00510h

rsc.li/nanoscale-advances

1. Introduction

Hydrogen fuel cell technology, an alternative to fossil fuels, requires abundant H_2 and O_2 production to meet energy requirements and acts as an efficient source of high-density energy (122 kJ g^{-1} of H_2).[1] Atmospheric air acts as the standard source of O_2 for fuel cells but for clean O_2 along with carbon-free H_2, electrochemical water splitting is favorable and can be optimized by using electrocatalysts.[2,3] Noble metals (Pt, Pd, Ru, Ir, and Rh) along with their compounds are promising electrocatalysts for hydrogen production, however, their limited occurrence and high cost impede their commercial use.[4] Various engineering strategies are being employed to develop transition metal-based metal–organic frameworks (MOFs),[3,5] carbides,[6] oxides,[7] chalcogenides,[8] phosphides,[9] borides,[10] alloys, *etc.* with modified morphologies, electronic structures, and defects for efficient H_2 and O_2 production. Nevertheless, electrochemical water splitting consumes a lot of energy due to sluggish kinetics, thermodynamic barriers, and catalyst limitations, posing a continuous challenge in developing electrocatalysts for large-scale industrial production of O_2 and H_2.[11] Among the metal carbides, molybdenum carbides (Mo_2C/MoC) have been examined for electrocatalytic water splitting owing to their Pt-like d-band electronic configuration, corrosion resistance, and high conductivities.[12,13] Heterostructures such as Mo_2C–MoS and Mo_2C–MoP have also been investigated to address these challenges, and these heterostructures have been seen to play a crucial role in the electrocatalytic properties of Mo_2C.[14,15] The high electron density on the d-orbital permits the easy Mo–H* bonding on the Mo_2C surface. Additionally, the carbon surrounding the Mo_2C/MoC plays a role in its catalytic activity, though it provides stability but also blocks the active sites on the surface of Mo. The interaction between the carbon's s and p orbitals and the d orbitals of molybdenum can be optimized by the introduction of *n*-type dopants (N, P, and S) which optimize H* bond interaction.[16,17] Similarly, group VIII metals can adjust the d-band center of Mo, which in turn reduces the Mo–H* bond energy and optimizes ΔGH* for MoC and Mo_2C, which boost their electrocatalytic activity.[18] Considering the effect of VIII metals and heteroatoms on molybdenum carbide, the Mo_xC heterostructure offers a solution, but this

Department of Chemistry, Quaid-i-Azam University, Islamabad-45320, Pakistan. E-mail: amir@qau.edu.pk; waqaslishah1@hotmail.com

† Electronic supplementary information (ESI) available. See DOI: https://doi.org/10.1039/d5na00510h

synergy must be strong enough to change the electron density and Gibbs free energies of adsorption and desorption of H*.[16,19]

Molybdenum carbides are less known for their oxygen evolution reaction (OER) activity because they are oxidized to molybdenum-based oxides and hydroxides that are soluble in the electrolyte. However, they have been reported to have good OER activity when their activity is enhanced through electronic synergistic and self-sacrificial effects of other transition elements (Fe, Co, Ni, *etc.*).[6,18,20] For instance, a pea-like CoP/Mo_2C compound was reported by Song and co-workers, exhibiting an overpotential of 265 mV for the OER at 10 mA cm^{-2}.[21] Similarly, the conversion of metallic atoms of transition elements to their sulfides and phosphides, when metal to sulfur/phosphorous (M : S/P) composition is properly adjusted, has an effect on boosting the overall water splitting performance and electrical conductivity of electrocatalysts.[22,23]

MOFs, due to their intrinsic porosity and rigid structure, when used as precursors offer an appropriate synthetic approach to prevent the unavoidable aggregation and excess growth of molybdenum carbide interfaces, while maintaining a high electrochemical surface area.[24,25] The highly porous crystalline structure of MOFs provides distinct advantages for creating nanostructured materials composed of carbon and/or metals. Porous carbons derived from MOFs are very promising for catalytic applications because they can inherit their high porosity, huge surface area, and great tailorability.[5,26]

Stimulated by the knowledge mentioned above, in this work, we used a NiCo-BTC MOF-assisted strategy to synthesize a group of electrocatalysts consisting of metallic (Ni and Co) phosphides, sulfides, and phosphosulfides doped on the Mo_2C–MoC heterostructure (Mo_xC) for overall water splitting. To achieve this, MoO_3 and NiCo-BTC were solvothermally combined to form a NiCo-BTC@MoO_3 composite that was carbonized in an Ar atmosphere to develop the Mo_2C–MoC heterostructure that obtained its carbon from the MOF's organic component, along with Ni and Co uniformly distributed in the conductive graphitic carbon on Mo_xC. The application of the host–guest relationship between the MOF and hydrothermally generated MoO_3, followed by carbonization allows an easy synthesis of NCMC. The resulting material was then subjected to sulfidation and phosphidation, individually and in combination, to produce electrocatalysts with enhanced performance. Benefiting from the S, P-doped porous carbon structure and the strong synergistic interaction between the Mo_2C–MoC heterostructure and metallic phosphosulfides, the tandem designed catalyst exhibits superior electrocatalytic activity for the hydrogen evolution reaction (HER) and OER under both acidic and basic conditions.[27]

2. Experimental section

2.1. Materials and chemicals

All the chemicals employed in this research are of analytical grade and do not require purification before use. $Ni(NO_3)_2 \cdot 6H_2O$, $Co(NO_3)_2 \cdot 6H_2O$, $(NH_4)_6Mo_7O_{24} \cdot 4H_2O$ (Sigma-Aldrich), trimesic acid (Macklin), KOH (EMSURE®), H_2SO_4 (Sigma-Aldrich), $NaH_2PO_2 \cdot H_2O$, S powder, conductive C black, aluminum oxide 0.05 μm (Electron Microscopy Sciences), Nafion™ perfluorinated resin solution (Sigma-Aldrich), *N*,*N*-dimethylformamide, methanol (C_2H_5OH), acidic acid CH_3COOH (Sigma-Aldrich), and ethylenediamine $C_2H_8N_2$ (DAEJUNG).

2.2. Synthesis of the NiCo-BTC MOF (NCMOF)

The NiCo-BTC MOF was synthesized through a solvothermal reaction (Fig. 1a). A solution of $Ni(NO_3)_2 \cdot 6H_2O$ (0.873 g, 3 mmol), $Co(NO_3)_2 \cdot 6H_2O$ (873 g, 3 mmol), and benzene tricarboxylic acid (0.63 g, 3 mmol) was prepared by dissolving them in a 50 mL mixture of DMF, ethanol, and water (4 : 1 : 1 v/v/v). To this solution, aqueous ethylenediamine was added dropwise to reach a pH of 8.7 and stirred for 10 min. After that 1 mL of acetic acid was added as a modulator. Subsequently, it was transferred to a Teflon-lined stainless-steel autoclave, where it was heated at 120 °C for 24 h, followed by cooling to ambient temperature.[28] After centrifugation and five ethanol washes, the violet-colored material was dried overnight at 60 °C.

2.3. Synthesis of the NiCo-BTC@MoO_3 composite (NCM)

$(NH_4)_6Mo_7O_{24} \cdot 4H_2O$ was placed in a crucible and heated at 450 °C to obtain MoO_3. NiCo-BTC (1.0 g) and MoO_3 (0.6 g) were dispersed in water and stirred. It was then transferred to an autoclave and heated at 120 °C for 6 h. The resulting material was subjected to centrifugation, repeatedly washed with water and C_2H_5OH, and dried to get MoO_3/NiCo-BTC (Fig. 1b).

2.4. Synthesis of NiCo–Mo_2C/MoC (NCMC) and NiCo@C (NCC)

The NiCo-BTC@MoO_3 was annealed in a quartz crucible by heating in a tube furnace under an argon flow (80 mL min^{-1}). The annealing process followed two sequential heating schemes: (1) the temperature was increased to 650 °C with a ramp rate of 5 °C min^{-1} and held at 650 °C for 3 h, and (2) subsequently raised to 850 °C at a ramp rate of 2 °C min^{-1} and maintained at that temperature for 3 h. The obtained black powder was identified as NiCo–Mo_2C/MoC and was labelled as NCMC. The same synthesis strategy, when applied to NiCo-MOF alone, yielded NiCo@C, labeled as NCC. Fig. 1c presents a schematic illustration for the synthesis of NiCo–Mo_2C/MoC.

2.5. Synthesis of NiS_2–CoS–Mo_xC (NCMCS)

Sulfur (1 g) and NiCo–Mo_2C/MoC (0.25 g) were placed in separate quartz crucibles inside a tube furnace and annealed at 450 °C for 4 h. The tube furnace temperature was raised to 450 °C at a ramp rate of 2 °C min^{-1} and an argon flow rate of 80 mL min^{-1} and maintained there for 4 h (Fig. 1d). After cooling the furnace to room temperature, the black product was collected. The resulting material, identified as NiS_2–CoS–Mo_xC, was labeled NCMCS. It was washed three times with water to remove any impurities and then dried overnight at 70 °C.

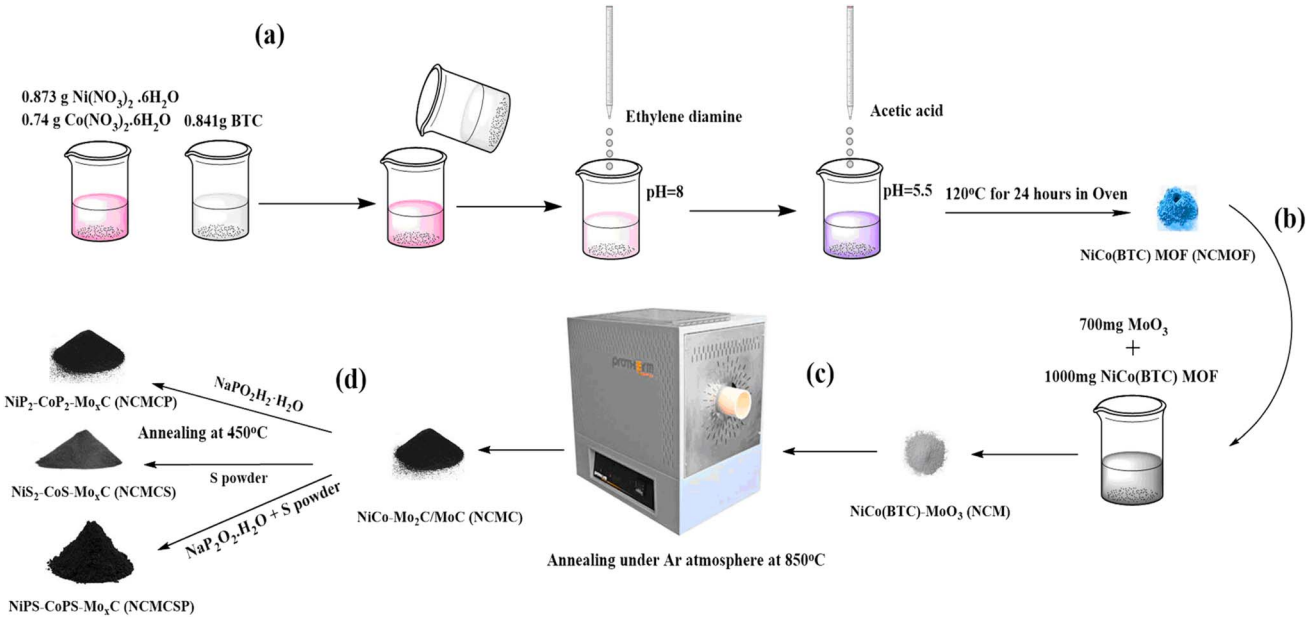

Fig. 1 (a) Synthesis scheme of NiCo-BTC MOF (NCMOF), (b) NiCo(BTC)-MoO_3 (NCM) composite, and (c) NiCo–MoC (NCMC) after annealing at 850 °C. (d) NCMCS, NCMCP, and NCMCSP.

2.6. Synthesis of NiP_2–CoP_2–Mo_xC (NCMCP)

$NaH_2PO_2 \cdot H_2O$ (2.0 g) and NiCo–Mo_2C/MoC (0.25 g) were placed in a tube furnace. The temperature was increased to 450 °C at a ramp rate of 2 °C min^{-1}, under an argon flow rate of 80 mL min^{-1}, and maintained for 4 hours (Fig. 1d). After the furnace was allowed to cool naturally, the black product, identified as NiP_2–CoP_2–Mo_xC, was obtained and labelled NCMCP. The material was then washed three times with water and dried overnight at 70 °C.

2.7. Synthesis of NiPS–CoPS–Mo_xC (NCMCSP)

$NaH_2PO_4 \cdot H_2O$ (2.0 g), sulfur (1.0 g), and NiCo–Mo_2C/MoC (0.25 g) were placed in a quartz crucible inside a tube furnace. The temperature was gradually raised to 450 °C at a ramp rate of 2 °C min^{-1} and held at that temperature for 4 hours (Fig. 1d). The resulting material was identified as NiPS–CoPS–Mo_xC and labelled NCMCSP. It was subsequently rinsed three times with water to remove any impurities and dried overnight at 70 °C.

3. Results and discussion

3.1. Materials characterization

The synthesis of NCMOF was confirmed *via* PXRD as shown in Fig. S1.† The XRD pattern appearing at $2\theta = 17.6°$, 18.7°, 26.7°, 27.4°, and 36° is indexed to (220), (111), (311), (202), and (440) planes respectively, for NiCo-BTC MOF (JCPDS card no. 96-702-6689).[29] Additionally, the NiCo-MOF exhibits characteristic peaks at $2\theta \approx 7.75°$, corresponding to $Ni_{7.2}Co_{4.8}$ $(BTC)_7$ MOF (JCPDS card no. 96-724-2988).[30] The synthesis of NCMC was validated through PXRD, with the pattern verifying the presence of MoC, Mo_2C, Co, and Ni (Fig. S2†) The diffraction peaks at $2\theta = 31.8°$, 35.7°, 48.6°, 64.2°, 66.5°, 73.5°, 75.7°, and 77.8° are indexed to the (001), (100), (101), (110), (002), and (111) planes of hexagonal MoC (JCPDS no. 03-065-6664).[31] Furthermore, the diffraction peaks at $2\theta \approx 34.5°$, 38.08°, 39.6°, 52.36°, 61.9°, 69.85° and 76° are indexed to the (100), (002), (101), (102), (110), (103), and (201) planes, attributed to β-Mo_2C with a hexagonal structure (JCPDS no. 03-065-8766).[32] The diffraction pattern at $2\theta = 44.60°$, 51.97°, and 76.6° corresponds to the (111), (200), and (220) planes of metallic Ni and Co (JCPDS card no. 01-070-0989 and 00-015-0806 respectively).

The sulfurization of NCMC results in the conversion of Ni and Co into NiS_2 and CoS respectively, with the final material being NCMCS. The formation of NiS_2 and CoS is confirmed from the PXRD pattern (Fig. 2a). The XRD peaks observed at 31.45°, 35.24°, 45.1°, and 53.3° correspond to the (200), (210), (220), and (311) planes of cubic NiS_2 (JCPDS card no. 01-088-1709). Similarly, the XRD peaks appear at 30.6°, 35.3°, 47.6°, and 54.4°, corresponding to the (100), (101), (102), and (110) crystal planes of CoS (JCPDS card no. 03-065-3418). Moreover, the phosphorization of NCMC results in the conversion of Ni and Co into NiP_2 and CoP_2 respectively to form NCMCP, the PXRD pattern for which is shown in Fig. 2b. Diffraction peaks appearing at 28.23°, 32.71°, 36.6°, 40.9°, 46.9°, and 55.6° are indexed to the (111), (200), (310), (211), (220), and (311) planes of NiP_2 (JCPDS card no. 01-073-0436). PXRD peaks at 24.45°, 32.01°, 36.6°, 35.8°, 37.21°, 39.21°, 39.4°, 51.6°, 51.9° and 58.54° are identified that are well indexed to the (111), (020), (002), (121), (012), (210), (113), (311), and (131) planes of monoclinic CoP_2 (JCPDS no. 00-026-0481). After simultaneous phosphorization and sulfurization of NCMC, the PXRD patterns match well with the crystal planes of NiPS and CoPS, with little variations (JCPDS cards 01-078-0499 and 00-027-0139, respectively) (Fig. 2c).

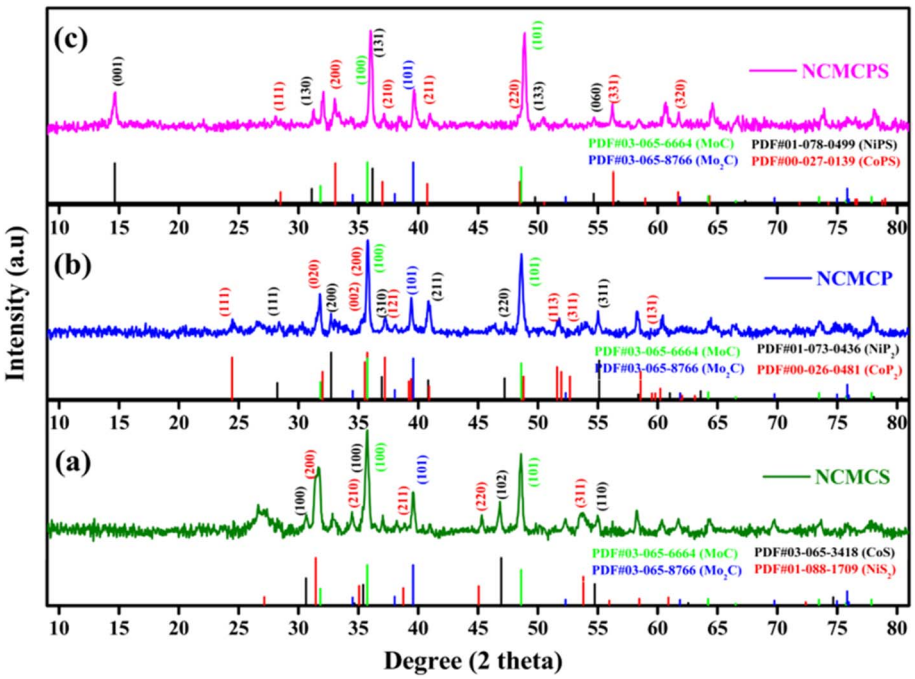

Fig. 2 XRD patterns of (a) NCMCS, (b) NCMCP, and (c) NCMCPS.

The XPS spectra analysis also confirms all the synthesized materials. Fig. 3a shows the survey scan of the materials after carbonization (NCMC) and subsequent sulfidation (NCMCS), phosphidation (NCMCP), and combined sulfo-phosphidation (NCMCSP). All the key elements are present, with their characteristic binding energies shown by shaded areas. The high-resolution XPS spectrum of Mo 3d in NCMCSP displays a doublet with peaks at 229 eV for $3d_{5/2}$ and 232.1 eV for $3d_{3/2}$ and shows the Mo–C bonds.[33,34] Additionally, two signals at 230 eV and 233.1 eV correspond to Mo^{+4} for $3d_{5/2}$ and $3d_{3/2}$ respectively, representing the Mo–O bond (Fig. 3b). A signal at 235.2 indicates the presence of a higher oxidation Mo–O bond due to surface oxidation. Another peak at 226.2 eV indicates the presence of sulfur (S 2s) due to the sulfidation process.[35] The Co 2p core region spectrum shows doublets at 779.9 eV and 795.1 eV for $2p_{3/2}$ and $2p_{1/2}$ of the Co–P bond, respectively and a small peak at 777 corresponds to reduced $Co\delta^0$.[36]

Similarly, another set of peaks at 782.4 eV and 797.9 eV for $2p_{3/2}$ and $2p_{1/2}$, respectively, indicates the presence of a Co–S bond.[37,38] Additionally, a broad shoulder corresponding to satellite peaks is observed at 785 eV and 803 eV (Fig. 3c). The core level spectrum of Ni 2p shows the split spin–orbit components for $2p_{3/2}$ and $2p_{1/2}$ for Ni–P (853.6 & 871.2 eV), Ni–S (854.5 & 872.1 eV), and Ni–O (856.3 & 874.1 eV) bonds, respectively (Fig. 3d) and the other shoulder peaks belong to satellite signals.[39,40] The most common oxidation state of Ni in Ni–S and N–P is +2. However, at a binding energy of 853.6 eV, $Ni^{\delta 0}$ may also be present, although it cannot be clearly distinguished from Ni–P. In the core level P 2p spectrum, a single peak was observed for the P–M bond which can be split into a closely spaced doublet at 129.9 and 130.8, attributed to P $2p_{3/2}$ and P $2p_{1/2}$ respectively (Fig. 3e) similar to previously reported studies.[40,41] The sulfur 2p core level spectrum can be deconvoluted into three peaks, with those at 161.6 eV and 162.8 eV corresponding to the 2p3/2 and 2p1/2 states, respectively, for S–M bonds (Fig. 3f). A third peak at 168.9 eV shows the presence of oxidized sulfur S–O bonds possibly due to sulfur oxidation.[37] The carbon 1 s high-resolution spectrum shows a peak around 282.5 eV for C–M bonds, and another peak at 284.2 eV for graphitic sp^2 carbon (Fig. 3g). Additionally, peaks were detected at 285.9 eV and 287.6 eV, corresponding to C–P and C–O bonds, respectively.[42]

The FESEM images of the pristine NCMOF (Fig. S3a and b†) reveal a sheet-like morphology with broad spike-like outgrowths on the sheets, which are interconnected to form larger structures. The SEM images confirmed the interesting morphology with a high surface exposure, which is beneficial for providing open spaces for ion adsorption and faster diffusion of electrolytes in and out of the MOF. MoO_3 loading and subsequent two step pyrolysis at 650 °C and 850 °C give NCMC, which exhibits a smooth surface with sheet-like morphology and small round shape outgrowths as displayed in Fig. 4a and b. The pyrolysis at 650 °C plays a role in retaining the morphology of the NCMOF part and avoiding aggregation into larger structures, and a heating temperature of 850 °C helps in the formation of the Mo_xC heterostructure. The structural morphology of NCMCSP exhibits porous, stacked, layered particles with irregular morphologies, as shown by the SEM images (Fig. 4c and d). The final nanosized morphology still offers abundant active sites for electrocatalytic-driven HER and OER. Fig. 4e shows the elemental mapping of the elements present after successful sulfidation and phosphidation (NCMCSP) and all the key elements Mo, Ni, Co, S, P, C are present. We are confident that the successful formation of carbon-confined NiPS and CoPS

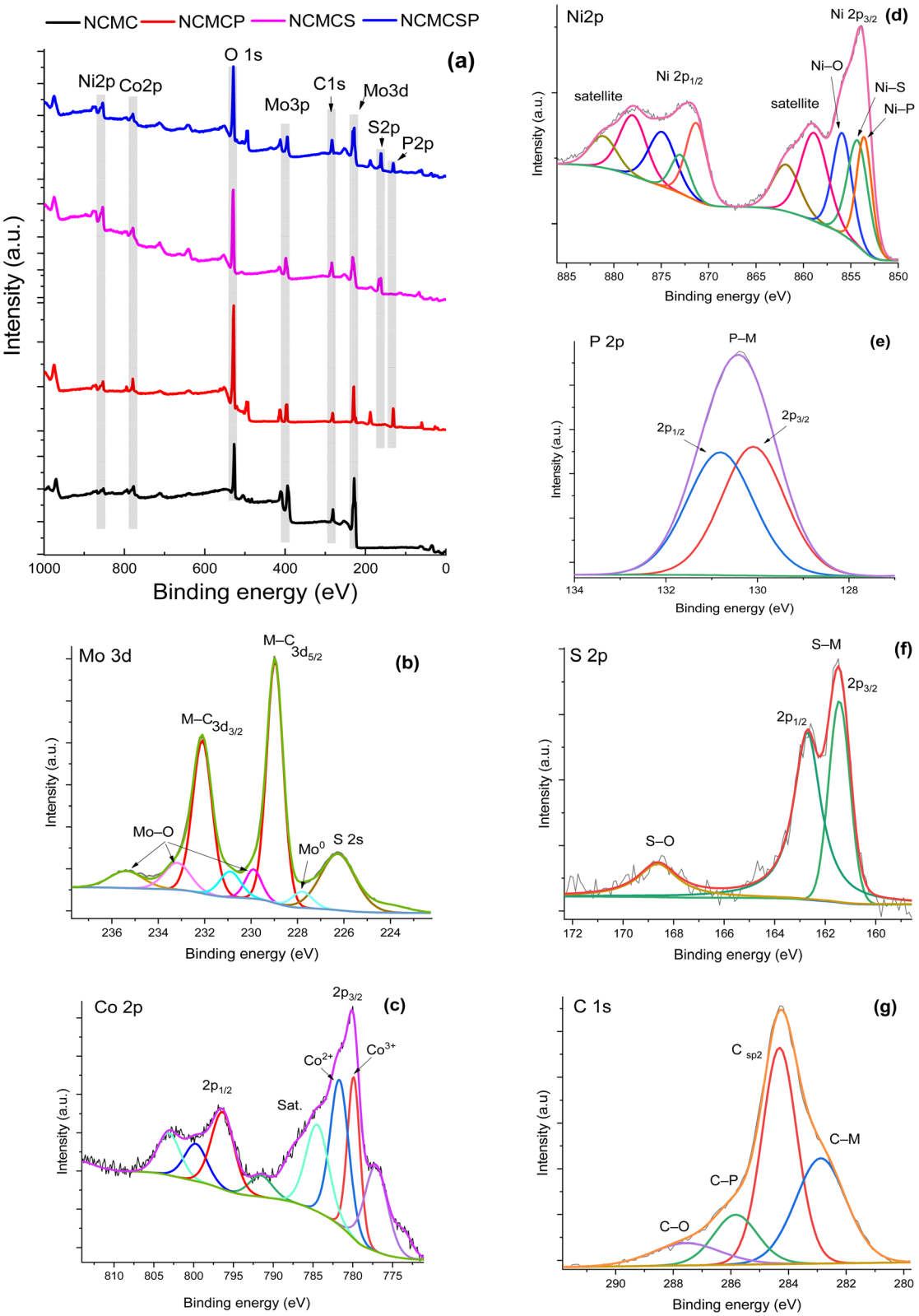

Fig. 3 XPS spectra: (a) survey scan of NCMCSP (blue), NCMCS (pink), NCMCP (red), and NCMC (black), and high-resolution scans of NCMCSP for (b) Mo 3d, (c) Co 2p, (d) Ni 2p, (e) P 2p, (f) S 2p, and (g) C 1s.

layers on the Mo_xC substrate is a direct consequence of the MOF matrix that effectively prevents the movement and aggregation of nanoparticles during high-temperature annealing. Fig. 4f shows the TEM images of NCMCSP, showing the presence of Mo_xC sheet like particles on which metal tiny sulfide/phosphide particles are visible (encircled).

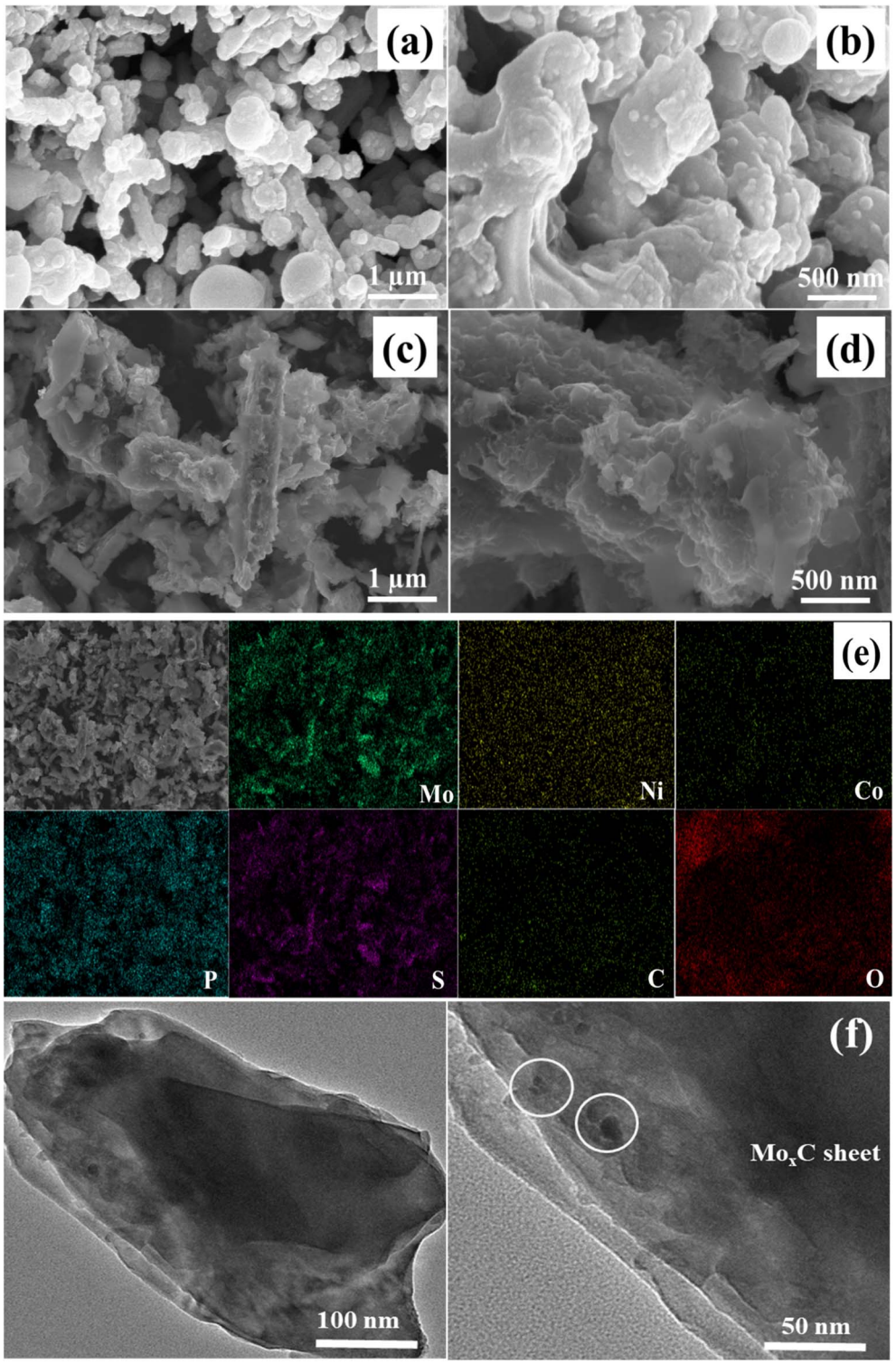

Fig. 4 FESEM images of NCMC (a and b) and NCMCSP (c and d). Elemental mapping of NCMCSP (e). TEM images (f).

3.2. Electrocatalytic activity measurements

The electrochemical experiments were conducted at room temperature utilizing the Electrochemical Workstation, Zennium Xc series. In the three-electrode setup, a platinum wire was used as the auxiliary electrode, a Ag/AgCl electrode saturated with KCl served as the reference electrode, and the working electrocatalyst was applied to a glassy carbon electrode (GCE) with a 5 mm diameter. For cleaning the GC electrodes, it was polished with alumina powder (0.05 μm particle size) until a fresh GC surface was obtained, followed by washing with deionized water and isopropanol for 15 minutes using

ultrasonication, and then allowed to air dry at room temperature. 5 mg of the sample was dispersed in a mixture of 50 μL of 20% Nafion solution, 150 μL of water, and 800 μL of propanol. It was sonicated until an evenly distributed suspension was formed. The sonicated slurry was applied to the GC electrode using a pipette and allowed to dry at room temperature. The catalyst mass loading was 0.255 mg cm^{-2}. Overpotential and Tafel slope calculations were made from LSV data. LSV measurements were performed at a scanning rate of 5 mV s^{-1} in 0.5 M H_2SO_4 and 1 M KOH electrolytes. The potential window used for the HER in 0.5 M H_2SO_4 and 1 M KOH was −0.5 V to 0.1 V and −0.6 V to 0.1 V *vs.* RHE, respectively; and 1 V to 1.8 V *vs.* RHE for the OER in alkaline medium. All the potentials were adjusted to the equivalent reversible hydrogen electrode (RHE) potential using the Nernst equation. The electrochemically active surface area (ECSA) was determined by measuring the double-layer capacitance (C_{dl}) using cyclic voltammetry (CV) within a non-faradaic potential range, with scan rates varying from 5 mV s^{-1} to 100 mV s^{-1}. For the 0.5 M H_2SO_4 solution, the chosen potential window was 0.15–0.25 V *versus* RHE, and for the 1 M KOH solution, it was 0.92–1.02 V *versus* RHE. To ascertain the electrocatalysts' charge transfer resistance, EIS was performed. It was carried out with an AC voltage of 5 mV at an overpotential of 100 mV against RHE in 1 M KOH and 0.5 M H_2SO_4, at a frequency range of 0.1 Hz to 100 kHz. Circuit fitting and charge transfer resistance (R_{ct}) calculations from EIS data were performed by using Zview software. The stability of the catalyst was assessed by a long period of CV to check the catalyst performance.

3.3. Electrocatalytic performance of catalysts

The electrocatalytic HER activities of NCC, NCMC, NCMCS, NCMCP, and NCMCSP drop-cast on a GCE were examined in acidic medium (0.5 M H_2SO_4). Initially, it was observed that the NCC exhibits activity for electrocatalytic hydrogen evolution but requires a high overpotential value of 260 mV to achieve a current density of 10 mA cm^{-2}. Fig. 5a displays the linear sweep voltammetry (LSV) polarization curves in 0.5 M H_2SO_4 (without iR correction). The NCMCSP electrocatalyst requires an overpotential (η_{10}) of 75.2 mV *vs.* RHE to deliver a cathodic current density of 10 mA cm^{-2}, significantly outperforming the HER overpotential of NCMCP, NCMCS, NCMC and NCC (η_{10} = 105.3, 122, 153.4 and 255 mV *vs.* RHE, respectively). The NCMCSP exhibits significantly superior performance compared to other Mo_xC-based materials and is competitive with Pt-based electrocatalysts for the HER.

The Tafel equation ($\eta = a + b \log j$, where j is the current density, a is a constant that characterizes the sensitivity of the current density to overpotential, b is the Tafel slope, and η represents the overpotential), is utilized to characterize the intrinsic kinetic processes associated with the HER. By extrapolating the linear section of the overpotential (η) *vs.* log$j$ graph (Fig. 5b), Tafel slopes of 57.3, 79.85, 87.29, 90.82, and 116.28 mV dec^{-1} (without iR correction) were determined for NCMCSP, NCMCP, NCMCS, NCMC, and NCC, respectively. The low Tafel slope for NCMCSP indicates highly efficient hydrogen evolution kinetics, suggesting a two-electron transfer process that follows a Volmer–Heyrovsky mechanism involving bimolecular

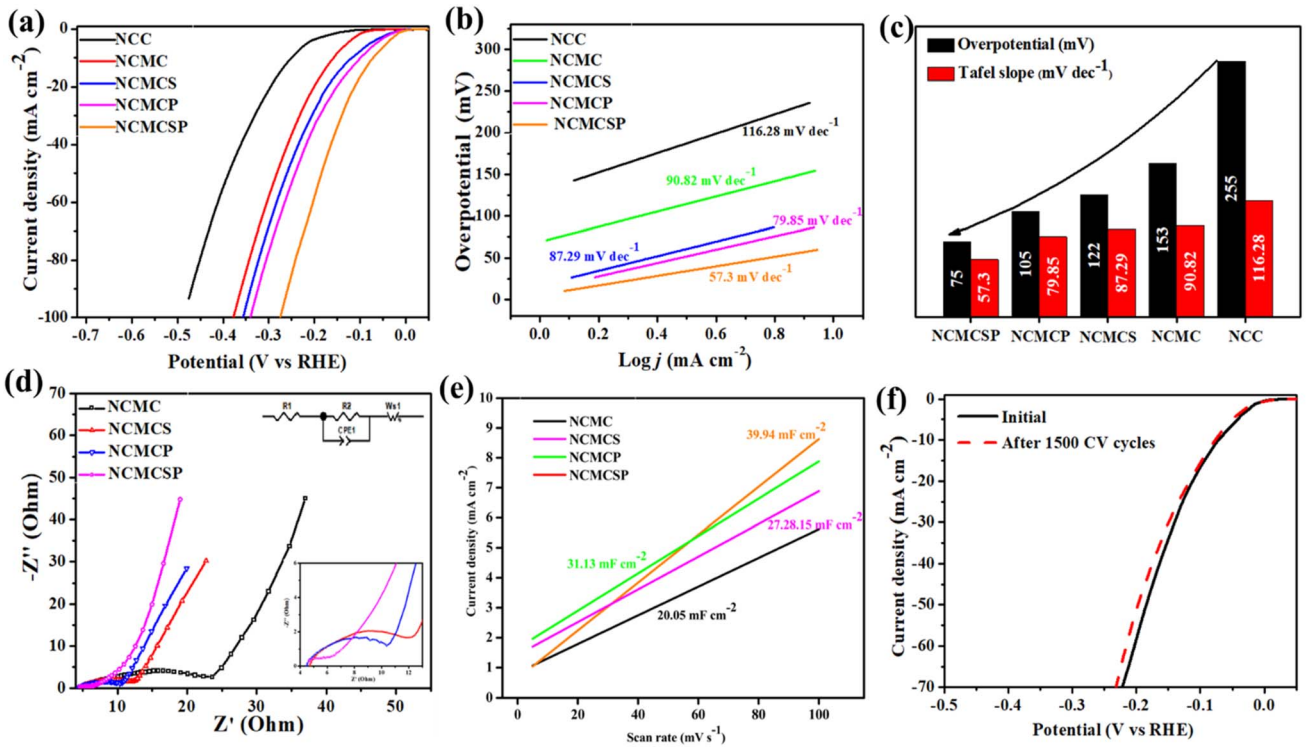

Fig. 5 (a) HER polarization curves, (b) Tafel curves in 0.5 M H_2SO_4, (c) comparison of overpotentials and Tafel slopes, (d) Nyquist plots, (e) double layer capacitance curves, and (f) HER polarization curves before and after 1500 CV cycles.

adsorption and hydrogen evolution. The high electron density of unoccupied d-orbitals permits strong Mo–H* binding on the Mo_2C surface and thus has negative hydrogen adsorption energy (ΔGH*).[43–45] This robust bonding enhances the effective adsorption of H* on the surface, allowing the initial proton reduction (Volmer step) to proceed rapidly. However, it restricts the desorption of H* from Mo_2C (Heyrosky/Tafel step), which greatly affects the kinetics of the HER.[46] Conversely, the electron density near the Fermi level of the Mo atom in MoC is transferred to the adjacent carbon atoms, reducing the ability of Mo to donate electrons to protons, which leads to slow kinetics in the Volmer step. Therefore, MoC with increased carbon content weakens the Mo–H* bond, facilitating a rapid Heyrovsky/Tafel step but hindering the Volmer step.[47,48] Considering the impact of individual molybdenum carbide, the heterostructure of Mo_2C and MoC offers a solution, but this synergy must be strong enough to modulate the electron density and Gibbs free energies of both H* adsorption and desorption.[16,19,49]

We additionally utilized electrochemical impedance spectroscopy (EIS) to gain a deeper understanding of the electrode kinetics during the HER. The Nyquist plots (Fig. 5d) were analyzed using an equivalent circuit (shown in Fig. 5d) to determine the R_{ct}. The plots confirm that the NCMCSP electrode exhibits a significantly lower R_{ct} value of 1.25 Ω at $\eta = 100$ mV compared to NCMCP (6.2 Ω), NCMCS (8.04 Ω), and NCMC (18.4 Ω), indicating a faster faradaic response and superior HER kinetics for NCMCSP. The surface characteristics of an electrocatalyst are crucial in determining its electrocatalytic performance. To assess this, the electrochemically active surface area (ECSA) of all electrocatalysts was determined through the C_{dl} derived from CV curves. Since C_{dl} is directly proportional to the electrochemically active surface area, CV testing was performed. The CV cycles performed for NCMCSP, NCMCP, NCMCS, and NCMC in the acidic medium are shown in Fig. S4(a–d).† As the scan rate increased from 5 mV s^{-1} to 100 mV s^{-1}, the capacitive currents showed a linear increase. For each CV cycle, the anodic and cathodic current densities at a potential of 0.20 V *vs.* RHE were measured. The difference, Δj, between the anodic and cathodic current densities was calculated, and a graph was plotted showing Δj against the scan rates. This linear fit of Δj *vs.* scan rates yielded a slope with double the value of C_{dl}. The C_{dl} value for NCMCSP was 39.94 mF cm^{-2}, which beats the values for NCMCP (31.13 mF cm^{-2}), NCMCS (27.28 mF cm^{-2}), and NCMC (20.05 mF cm^{-2}) (Fig. 5e). This indicates that NCMCSP has a large catalytic surface area, providing more active sites for the HER. Accordingly, ECSAs are 501.25 cm^2 for NCMC, 682 cm^2 for NCMCS, 778.25 cm^2 for NCMCP, and 998.5 cm^2 for NCMCSP (ESI Table S1†). Thus, NCMCSP demonstrates the highest ECSA, which positively impacts its catalytic performance. Furthermore, the long-term durability of NCMCSP was assessed through 1500 CV cycles, demonstrating that the electrocatalyst maintains a high current

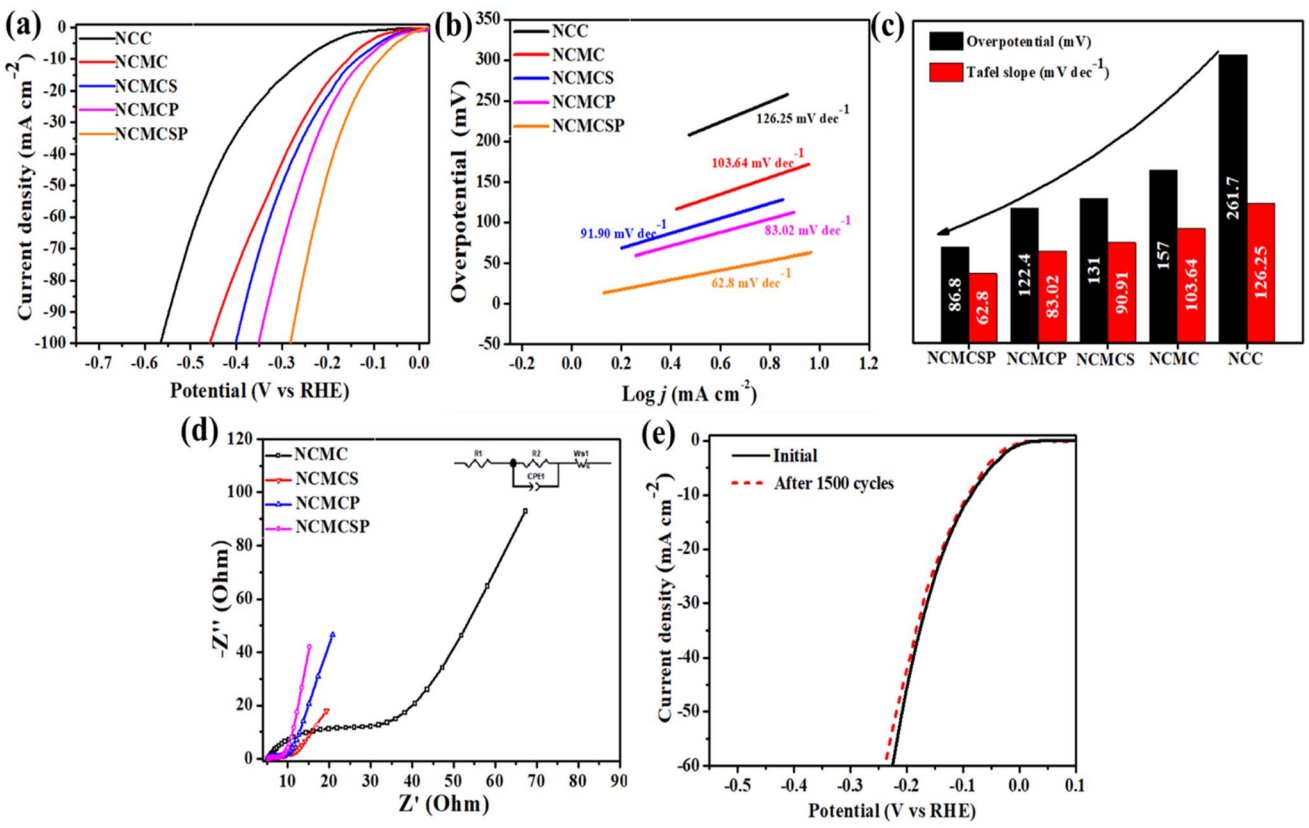

Fig. 6 (a) HER polarization curves, (b) the corresponding Tafel curves, (c) comparison of overpotentials and Tafel slopes, (d) Nyquist plots, and (e) HER polarization curves before and after 1500 CV cycles.

density with only a 7 mV increase in overpotential at 10 mA cm^{-2} (Fig. 5f), confirming its excellent durability for HER applications.

The electrocatalytic performance for the HER of the molybdenum–carbide-based rod structures was assessed in a basic aqueous solution (1 M KOH), with all potentials (overpotentials) reported relative to the RHE. The associated LSV HER polarization curves are presented in Fig. 6a, revealing a noteworthy trend: NCMCSP > NCMCP > NCMCS > NCMC > NCC. As shown in Fig. 6a, η_{10} values are 86.8, 122.4, 131, 157, and 261.7 mV for NCMCSP, NCMCP, NCMCS, NCMC, and NCC, respectively, with corresponding Tafel slopes of 62.8, 83.02, 90.91, 103.64, and 126.25 mV dec^{-1} (Fig. 6b). This suggests that dual doping with P and S likely plays a crucial role in the adsorption and desorption of atomic H. This aligns with previous studies indicating that the presence of both phosphorus and sulfur can enhance catalytic activity for the HER due to a synergistic effect between the two elements.[27] To gain insight into the fundamental origins, EIS analysis was conducted at a selected overpotential ($\eta = 100$ mV) on these catalysts. The Nyquist plots (Fig. 6d) were fitted employing an equivalent circuit (inset in Fig. 6d) to determine the R_{ct}, which measured 3.8, 4.47, 5.74, and 28.66 Ω for NCMCSP, NCMCP, NCMCS, and NCMC, respectively. These results indicate a faster faradaic response and thus superior HER kinetics for NCMCSP, with a higher number of electrons transferred at a current density of 10 mA cm^{-2}. The R_{ct} value for NCMCSP was significantly lower than those for NCMCP, NCMCS, and NCMC at the same overpotential, aligning well with their varying HER activities. The reduced charge transfer resistance is mainly attributed to the strong synergistic interactions among the MoC_x nanocrystallites, NiCoPS, and the incorporated carbon matrix. Long-term stability of NCMCSP was also evaluated for application in large-scale industrial water electrolysis. 1500 CV cycles were conducted to evaluate the stability of NCMCSP in KOH solution, revealing a minor increase of 6 mV in the overpotential (Fig. 6e) confirming its robustness.

To assess the OER activity of the synthesized catalysts, measurements were taken for overpotential, Tafel slope, and

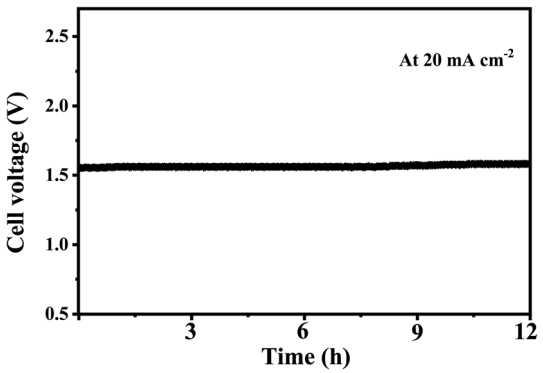

Fig. 8 Overall water splitting performance of NCMCSP during a 12 h chronopotentiometry test.

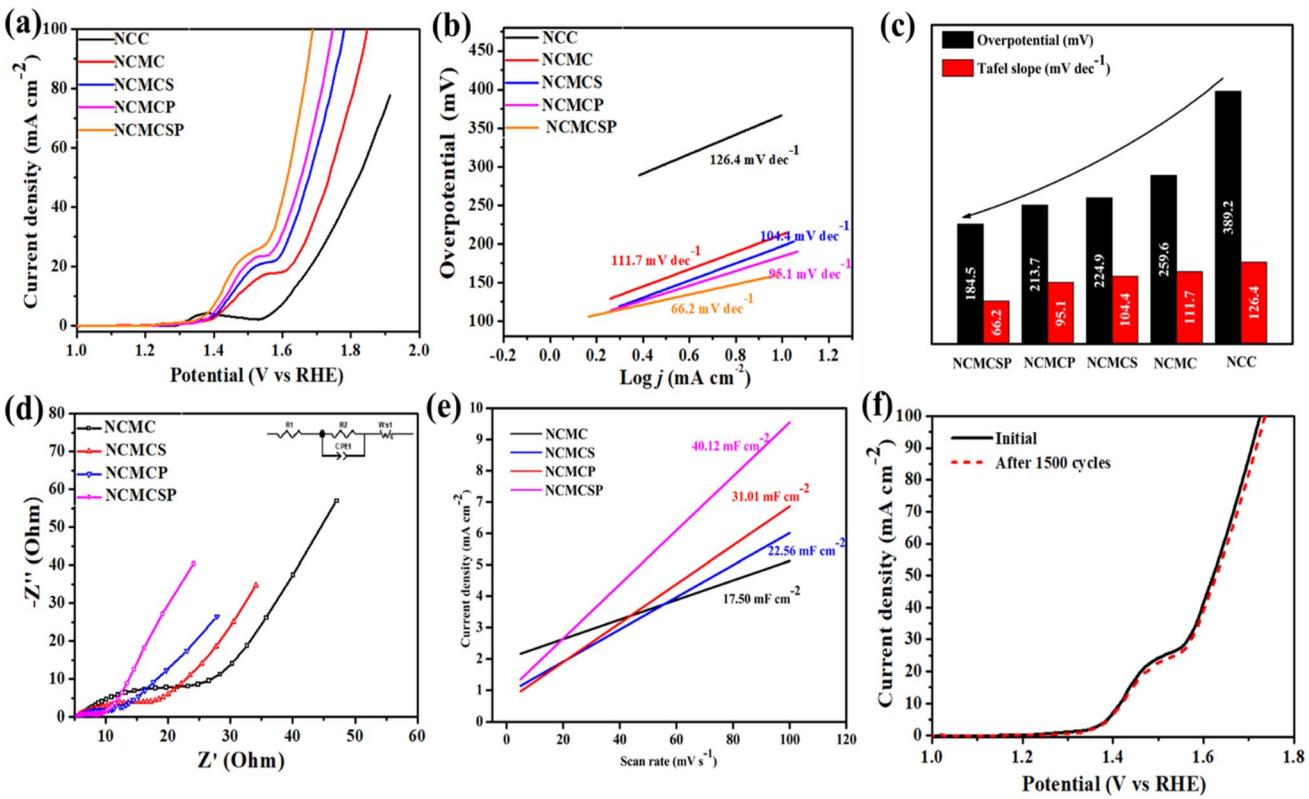

Fig. 7 (a) OER polarization curves, (b) the corresponding Tafel curves, (c) comparison of overpotential values and Tafel slopes, (d) Nyquist plots, (e) double layer capacitance curves, and (f) OER polarization curves for NCMCSP before and after 1500 CV cycles.

Table 1 HER and OER overpotentials of NCMC, NCMCS, NCMCP and NCMCSP at an overpotential of 10 mA cm^{-2} (η_{10}), 20 mA cm^{-2} (η_{20}) and 100 mA cm^{-2} (η_{100}) in 0.5 M H_2SO_4 and 1 M KOH

	HER overpotential (mV) in 0.5 M H_2SO_4			HER overpotential (mV) in 1 M KOH			OER overpotential (mV) in 1 M KOH		
Catalysts	η_{10}	η_{20}	η_{100}	η_{10}	η_{20}	η_{100}	η_{10}	η_{20}	η_{100}
NCMCSP	75.2	110.5	275.1	86.8	130.8	291.7	184.5	238.7	459.2
NCMCP	105.3	154.2	340.2	122.4	177	352.8	213.7	268.6	519.3
NCMCS	122	172.02	357.2	131	192.2	402	224.9	299.4	559.2
NCMC	153.4	205	389.8	157	227.3	467.1	259.6	394.5	620.5

charge transfer resistance. The OER polarization curves of the catalysts are shown in Fig. 7a. NCMCSP exhibited enhanced OER activity compared to NCMCP, NCMCS, NCMC, and NCC. For instance, NCMCSP needed an overpotential of 184.5 mV for a current density of 10 mA cm^{-2}, significantly superior to NCMCP, NCMCS, NCMC, and NCC which required overpotential values of 213.7, 224.9, 259.6, and 389.2 mV respectively to reach the same current density. The reduction peak at a potential of 1.4–1.5 V *vs.* RHE corresponds to the oxidation peak of Ni^{2+} to Ni^{3+}, and the high current density obtained at the potential for NCMCSP, NCMCP, NCMCS and NCMC relative to NCC specifies better synergistic effects of MoC_x with NiCo (SP, P, and S) components. Additionally, the OER polarization curve for NCMCSP exhibits a higher current density at the same overpotential compared to the other synthesized catalysts. The Tafel slope values for NCMCSP, NCMCP, NCMCS, NCMC, and NCC calculated at a current density of 10 mA cm^{-2} are 66.2, 95.1, 104.4, 111.7, and 126.4 mV dec^{-1}, respectively. The Tafel slopes for OER activity in 1 M KOH are shown in Fig. 7b. Pt has a much lower Tafel slope value than the other electrocatalysts, indicating a faster reaction rate. The improved HER performance of phosphides and sulfides is attributed to the high electronegativity and electron density on P and S, which enhance their ability to capture proton and promote catalysis.[50–52] Similarly, metal phosphides and sulfides show great potential as OER electrocatalysts because they form oxo/hydroxo active sites on their surfaces, which collectively expedite the conversion of OH* to OOH* and subsequently to O_2.[52,53] EIS was performed to determine the kinetics and charge transfer studies of the materials in 1 M KOH. R_{ct} represents the impedance faced by electrocatalysts during electron transfer to the substrate. In this study, EIS was conducted at an overpotential of 250 mV (*vs.* RHE) over a frequency range of 0.1 Hz to 100 kHz using an AC voltage of 5 mV. Fig. 7d presents the equivalent circuit diagram and Nyquist plot for NCMCSP, NCMCP, NCMCS, NCMC, and NCC in 1 M KOH. The Nyquist plots demonstrate that NCMCSP exhibits the lowest charge transfer resistance of 3.1 Ω, which is significantly lower than that of NCMCP (4.8 Ω), NCMCS (11.8 Ω), and NCMC (23.92 Ω). The lower R_{ct} value for NCMCSP correlates with its superior HER activity and more efficient reaction kinetics.

CV was conducted in the potential window 0.92–1.02 V *vs.* RHE for NCMCSP, NCMCP, NCMCS, and NCMC in 1 M KOH as shown in Fig. S5(a–d).† The anodic and cathodic current densities were measured at a potential of 0.98 V *versus* RHE for each CV cycle. From these measurements, the calculated C_{dl} values in 1 M KOH are 40.12, 31.01, 22.56, and 17.5 mF cm^{-2} for NCMCSP, NCMCP, NCMCS, and NCMC (Fig. 7e) respectively. This indicates that NCMCSP provides enhanced exposure of active catalytic sites on the surface. Accordingly, the electrochemically active surface areas (ECSAs) were estimated to be 437.5 cm^2 for NCMC, 564 cm^2 for NCMCS, 775.25 cm^2 for NCMCP, and 1003.25 cm^2 for NCMCSP (ESI Table S2†). Therefore, NCMCSP possesses the largest ECSA, which contributes to its higher catalytic efficiency for the HER. The long-term OER durability of the NCMCSP electrode was also examined by subjecting it to 1500 CV cycles at an overpotential of 250 mV in 1 M KOH. After these cycles, the η_{10} value increased only slightly from 238.7 mV to 243 mV, indicating a minimal shift in the LSV polarization curve (Fig. 7f). This result confirms the long-term stability and robustness of NCMCSP as an effective OER electrocatalyst.

The performance of the NCMCSP electrocatalyst as both the anode and cathode was evaluated for overall water splitting in 1 M KOH solution. The durability of the NCMCSP-based electrolyzer for the overall water splitting was also evaluated by measuring the voltage over time at a constant current density of 20 mA cm^{-2} for 12 h, as shown in Fig. 8. The performance of the NCMCSP electrolyzer was maintained (98.4%) without any noticeable deterioration during the durability test, proving its high activity and stability during the overall water splitting. Table 1 shows the overpotential values of all the catalysts prepared at current densities of 10, 20 and 100 mA cm^{-2} (η_{100}) in 0.5 M H_2SO_4 and 1 M KOH for OER and HER activities. It can be seen that high current densities can be achieved with lower overpotentials under acidic as well as under alkaline conditions. In addition to that, ESI Tables S3, S4, and S5† show that the NiPS–CoPS–Mo_xC electrocatalysts developed in this research reveal augmented activity compared to previously reported Mo_xC-based electrocatalysts for HER and OER studies.

4. Conclusion

In summary, we successfully prepared NiPS–CoPS–Mo_xC (NiPS and CoPS supported on Mo_2C–MoC nanorods) from a NiCo-MOF@MoO_3 composite through carbonization followed by phosphosulfurization. The Mo_2C–MoC heterostructure, along with metallic phosphosulfides, a large electrochemically active surface area, and enhanced stability imparted by the porous carbon matrix, enables the synthesized NiPS–CoPS–Mo_xC to

exhibit excellent electrocatalytic performance for the HER and OER under acidic and alkaline conditions. It achieves a catalytic current density of 10 mA cm^{-2} at an overpotential of 184.5 mV *vs.* RHE and a Tafel slope of 66.2 mV dec^{-1} in 1 M KOH for the OER. This electrocatalyst also delivers enhanced hydrogen evolution activity, demonstrated by a low overpotential of 75.2 mV in 0.5 M H_2SO_4 and 86.8 mV in 1 M KOH, with corresponding Tafel slopes of 57.3 mV dec^{-1} and 62.8 mV dec^{-1}, respectively. This work demonstrates the potential of tailored heterostructures for next-generation energy conversion technologies. We believe our research introduces an innovative and effective strategy for developing noble-metal-free electrocatalysts aimed at the sustainable production of green hydrogen.

Data availability

The data supporting this article have been included as part of the ESI.†

Conflicts of interest

There is no conflicts to declare.

Acknowledgements

The authors are grateful to the Pakistan Science Foundation for financial assistance under project no. PSF-NSFC-IV/Chem/C-QAU (27).

References

1 O. Z. Sharaf and M. F. Orhan, An overview of fuel cell technology: fundamentals and applications, *Renewable Sustainable Energy Rev.*, 2014, **32**, 810–853.
2 Y. Luo, Z. Zhang, M. Chhowalla and B. Liu, Recent advances in design of electrocatalysts for high-current-density water splitting, *Adv. Mater.*, 2022, **34**, 2108133.
3 N. Sun, S. S. A. Shah, Z. Lin, Y.-Z. Zheng, L. Jiao and H.-L. Jiang, MOF-Based Electrocatalysts: An Overview from the Perspective of Structural Design, *Chem. Rev.*, 2025, **125**(5), 2703–2792.
4 Y. Li, Y. Sun, Y. Qin, W. Zhang, L. Wang, M. Luo, H. Yang and S. Guo, Recent advances on water-splitting electrocatalysis mediated by noble-metal-based nanostructured materials, *Adv. Energy Mater.*, 2020, **10**, 1903120.
5 A. Areeb Amjad, M. Murtaza, S. Shoaib Ahmad Shah, I. Ahmad, H. Alawadhi, W. Ali Shah and A. Waseem, Atomically precise MOF-Based electrocatalysts by design: Hydrogen evolution applications, *Fuel*, 2025, **385**, 134021.
6 M. S. A. Sher Shah, G. Y. Jang, K. Zhang and J. H. Park, Transition metal carbide-based nanostructures for electrochemical hydrogen and oxygen evolution reactions, *EcoEnergy*, 2023, **1**, 344–374.
7 A. S. Jamadar, R. Sutar, S. Patil, R. Khandekar and J. B. Yadav, Progress in metal oxide-based electrocatalysts for sustainable water splitting, *Mater. Rep.: Energy*, 2024, 100283.
8 X. Duan, J. Xu, Z. Wei, J. Ma, S. Guo, H. Liu and S. Dou, Atomically thin transition-metal dichalcogenides for electrocatalysis and energy storage, *Small Methods*, 2017, **1**, 1700156.
9 Y. Lee, W. Jeong, Y. J. Hwang, B. An, H. Lee, H. Jeong, G. Kim, Y. Park, M. Kim and D.-H. Ha, Basics, developments, and strategies of transition metal phosphides toward electrocatalytic water splitting: beyond noble metal catalysts, *J. Mater. Chem. A*, 2024, **12**, 28574–28594.
10 S. Gupta, M. K. Patel, A. Miotello and N. Patel, Metal boride-based catalysts for electrochemical water-splitting: A review, *Adv. Funct. Mater.*, 2020, **30**, 1906481.
11 M. Du, F. Yu, S. Gong and F. Liu, Design of Electrocatalysts with High Performance Based on Thermodynamics and Kinetics: Progress and Prospects, *Adv. Funct. Mater.*, 2024, 2413826.
12 J. Wan, Q. Liu, T. Wang, H. Yuan, P. Zhang and X. Gu, Theoretical investigation of platinum-like catalysts of molybdenum carbides for hydrogen evolution reaction, *Solid State Commun.*, 2018, **284**, 25–30.
13 J. R. dos Santos Politi, F. Vines, J. A. Rodriguez and F. Illas, Atomic and electronic structure of molybdenum carbide phases: bulk and low Miller-index surfaces, *Phys. Chem. Chem. Phys.*, 2013, **15**, 12617–12625.
14 C. Zhang, Z. Pan and Y. Tao, Synthesis and Catalytic Performance of Mo_2C/MoS_2 Composite Heterojunction Catalysts, *Materials*, 2024, **17**, 2355.
15 Y. Zhan, F. Xie, H. Zhang, Z. Lin, J. Huang, W. Zhang, X. Sun, H. Meng, Y. Zhang and J. Chen, Metallic Ni promoted Mo_2C–MoN particles supported on N-doped graphitic carbon as bifunctional catalyst for oxygen and hydrogen evolution reaction in alkaline media, *J. Electrochem. Soc.*, 2018, **165**, F75.
16 Q. Gao, W. Zhang, Z. Shi, L. Yang and Y. Tang, Structural design and electronic modulation of transition-metal-carbide electrocatalysts toward efficient hydrogen evolution, *Adv. Mater.*, 2019, **31**, 1802880.
17 L. Ji, J. Wang, X. Teng, H. Dong, X. He and Z. Chen, N, P-doped molybdenum carbide nanofibers for efficient hydrogen production, *ACS Appl. Mater. Interfaces*, 2018, **10**, 14632–14640.
18 Y. Xu, J. Yang, T. Liao, R. Ge, Y. Liu, J. Zhang, Y. Li, M. Zhu, S. Li and W. Li, Bifunctional water splitting enhancement by manipulating Mo–H bonding energy of transition Metal–Mo_2C heterostructure catalysts, *Chem. Eng. J.*, 2022, **431**, 134126.
19 H. Lin, Z. Shi, S. He, X. Yu, S. Wang, Q. Gao and Y. Tang, Heteronanowires of MoC–Mo_2C as efficient electrocatalysts for hydrogen evolution reaction, *Chem. Sci.*, 2016, **7**, 3399–3405.
20 B. Geng, F. Yan, L. Liu, C. Zhu, B. Li and Y. Chen, Ni/MoC heteronanoparticles encapsulated within nitrogen-doped carbon nanotube arrays as highly efficient self-supported electrodes for overall water splitting, *Chem. Eng. J.*, 2021, **406**, 126815.

21 S. Dutta, A. Indra, H. Han and T. Song, An Intriguing Pea-Like Nanostructure of Cobalt Phosphide on Molybdenum Carbide Incorporated Nitrogen-Doped Carbon Nanosheets for Efficient Electrochemical Water Splitting, *ChemSusChem*, 2018, **11**, 3956–3964.

22 N. Jiang, Q. Tang, M. Sheng, B. You, D.-e. Jiang and Y. Sun, Nickel sulfides for electrocatalytic hydrogen evolution under alkaline conditions: a case study of crystalline NiS, NiS_2, and Ni_3S_2 nanoparticles, *Catal. Sci. Technol.*, 2016, **6**, 1077–1084.

23 P. Li and H. C. Zeng, Advanced oxygen evolution catalysis by bimetallic Ni–Fe phosphide nanoparticles encapsulated in nitrogen, phosphorus, and sulphur tri-doped porous carbon, *Chem. Commun.*, 2017, **53**, 6025–6028.

24 S. Chen, J. Xu, J. Chen, Y. Yao and F. Wang, Current Progress of Mo-Based Metal Organic Frameworks Derived Electrocatalysts for Hydrogen Evolution Reaction, *Small*, 2024, **20**, 2304681.

25 M. Murtaza, K. Farooq, A. A. Amjad, S. S. A. Shah and A. Waseem, Bimetallic Fe/Ni-BTC MOF decorated MXene hybrid for improved oxidation of water, *Diamond Relat. Mater.*, 2024, **147**, 111379.

26 Y.-Z. Chen, R. Zhang, L. Jiao and H.-L. Jiang, Metal–organic framework-derived porous materials for catalysis, *Coord. Chem. Rev.*, 2018, **362**, 1–23.

27 S. Park, J. Y. Kim and D. Yun Youn, Phase-engineered molybdenum carbide embedded in nitrogen-doped carbon nanofiber composites for enhanced hydrogen evolution, *J. Electroanal. Chem.*, 2025, 119187.

28 H. Guo, Y. Zhu, S. Wang, S. Su, L. Zhou and H. Zhang, Combining coordination modulation with acid–base adjustment for the control over size of metal–organic frameworks, *Chem. Mater.*, 2012, **24**, 444–450.

29 M. A. Nadeem, M. Bhadbhade and J. A. Stride, Four new coordination polymers constructed from benzene tricarboxylic acid: synthesis, crystal structure, thermal and magnetic properties, *Dalton Trans.*, 2010, **39**, 9860–9865.

30 B.-B. Yu, Y.-W. Hua, Q. Huang, S.-Y. Ye, H.-D. Zhang, Z. Yan, R.-W. Li, J. Wu, Y. Meng and X. Cao, Two-dimensional stable and ultrathin cluster-based metal–organic layers for efficient electrocatalytic water oxidation, *CrystEngComm*, 2021, **23**, 4700–4707.

31 E. Clougherty, K. Lothrop and J. Kafalas, A new phase formed by high-pressure treatment: face-centred cubic molybdenum monocarbide, *Nature*, 1961, **191**, 1194.

32 K. Madhav Reddy, T. N. Rao, J. Revathi and J. Joardar, Structural stability of α/β-Mo2C during thermochemical processing, *J. Alloys Compd.*, 2010, **494**(1–2), 386–391.

33 A. Kurlov, E. B. Deeva, P. M. Abdala, D. Lebedev, A. Tsoukalou, A. Comas-Vives, A. Fedorov and C. R. Müller, Exploiting two-dimensional morphology of molybdenum oxycarbide to enable efficient catalytic dry reforming of methane, *Nat. Commun.*, 2020, **11**, 4920.

34 M. Murtaza, K. Farooq, W. A. Shah, I. Ahmad and A. Waseem, Layered MOF supported on 2D delaminated MXene ($Mo_2Ti_2C_3$) nanosheets boosted water splitting, *Nanoscale Adv.*, 2024, **6**, 6317–6327.

35 F. Gong, S. Ye, M. Liu, J. Zhang, L. Gong, G. Zeng, E. Meng, P. Su, K. Xie, Y. Zhang and J. Liu, Boosting electrochemical oxygen evolution over yolk-shell structured O–MoS_2 nanoreactors with sulfur vacancy and decorated Pt nanoparticles, *Nano Energy*, 2020, **78**, 105284.

36 M. Murtaza, K. Farooq, W. A. Shah and A. Waseem, CoBDC MOF derived CoP/C couple with 2D Nb_2CT_x MXene as an efficient bifunctional catalyst for water splitting, *Fuel*, 2025, **394**, 135095.

37 Y. Du, W. Wang, H. Zhao, X. Jiang, Y. Liu, R. Chen, B. Yang and L. Wang, Activating CoMoS with CoP_3 Phase for High-efficient Hydrogen Evolution Reaction in Acidic Condition, *ChemCatChem*, 2021, **13**, 1362–1367.

38 K. Farooq, M. Murtaza, Z. Yang, A. Waseem, Y. Zhu and Y. Xia, MXene boosted MOF-derived cobalt sulfide/carbon nanocomposites as efficient bifunctional electrocatalysts for OER and HER, *Nanoscale Adv.*, 2024, **6**, 3169–3180.

39 X. Ding, D. Liu, P. Zhao, X. Chen, H. Wang, F. E. Oropeza, G. Gorni, M. Barawi, M. García-Tecedor, V. A. de la Peña O'Shea, J. P. Hofmann, J. Li, J. Kim, S. Cho, R. Wu and K. H. L. Zhang, Dynamic restructuring of nickel sulfides for electrocatalytic hydrogen evolution reaction, *Nat. Commun.*, 2024, **15**, 5336.

40 F. Poureshghi, F. Seland, J. O. Jensen and S. Sunde, Nickel Phosphide: The Effect of Phosphorus Content on the Activity and Stability toward Oxygen Evolution Reaction in Alkaline Medium, *ChemSusChem*, 2025, **18**, e202401586.

41 M. R. Kandel, U. N. Pan, P. P. Dhakal, R. B. Ghising, S. Sidra, D. H. Kim, N. H. Kim and J. H. Lee, Manganese-Doped Bimetallic $(Co,Ni)_2P$ Integrated CoP in N,S Co-Doped Carbon: Unveiling a Compatible Hybrid Electrocatalyst for Overall Water Splitting, *Small*, 2024, **20**, 2307241.

42 J. Wu, X. Zheng, C. Jin, J. Tian and R. Yang, Ternary doping of phosphorus, nitrogen, and sulfur into porous carbon for enhancing electrocatalytic oxygen reduction, *Carbon*, 2015, **92**, 327–338.

43 M. Miao, J. Pan, T. He, Y. Yan, B. Y. Xia and X. Wang, Molybdenum carbide-based electrocatalysts for hydrogen evolution reaction, *Chem. – Eur. J.*, 2017, **23**, 10947–10961.

44 J. R. Kitchin, J. K. Nørskov, M. A. Barteau and J. G. Chen, Trends in the chemical properties of early transition metal carbide surfaces: A density functional study, *Catal. Today*, 2005, **105**, 66–73.

45 Z. Shi, K. Nie, Z.-J. Shao, B. Gao, H. Lin, H. Zhang, B. Liu, Y. Wang, Y. Zhang and X. Sun, Phosphorus-Mo_2C@ carbon nanowires toward efficient electrochemical hydrogen evolution: composition, structural and electronic regulation, *Energy Environ. Sci.*, 2017, **10**, 1262–1271.

46 Z. W. Seh, K. D. Fredrickson, B. Anasori, J. Kibsgaard, A. L. Strickler, M. R. Lukatskaya, Y. Gogotsi, T. F. Jaramillo and A. Vojvodic, Two-dimensional molybdenum carbide (MXene) as an efficient electrocatalyst for hydrogen evolution, *ACS Energy Lett.*, 2016, **1**, 589–594.

47 X. Ji, K. Wang, Y. Zhang, H. Sun, Y. Zhang, T. Ma, Z. Ma, P. Hu and Y. Qiu, MoC based Mott–Schottky electrocatalyst for boosting the hydrogen evolution reaction performance, *Sustainable Energy Fuels*, 2020, **4**, 407–416.

48 Y. Ma, G. Guan, X. Hao, J. Cao and A. Abudula, Molybdenum carbide as alternative catalyst for hydrogen production–A review, *Renewable Sustainable Energy Rev.*, 2017, **75**, 1101–1129.

49 C. Liu, L. Sun, L. Luo, W. Wang, H. Dong and Z. Chen, Integration of Ni doping and a Mo_2C/MoC heterojunction for hydrogen evolution in acidic and alkaline conditions, *ACS Appl. Mater. Interfaces*, 2021, **13**, 22646–22654.

50 Y. Pan, Y. Liu, J. Zhao, K. Yang, J. Liang, D. Liu, W. Hu, D. Liu, Y. Liu and C. Liu, Monodispersed nickel phosphide nanocrystals with different phases: synthesis, characterization and electrocatalytic properties for hydrogen evolution, *J. Mater. Chem. A*, 2015, **3**, 1656–1665.

51 S. Anantharaj, S. R. Ede, K. Sakthikumar, K. Karthick, S. Mishra and S. Kundu, Recent Trends and Perspectives in Electrochemical Water Splitting with an Emphasis on Sulfide, Selenide, and Phosphide Catalysts of Fe, Co, and Ni: A Review, *ACS Catal.*, 2016, **6**, 8069–8097.

52 P. Liu and J. A. Rodriguez, Catalysts for hydrogen evolution from the [NiFe] hydrogenase to the Ni_2P (001) surface: the importance of ensemble effect, *J. Am. Chem. Soc.*, 2005, **127**, 14871–14878.

53 R. He, X. Huang and L. Feng, Recent Progress in Transition-Metal Sulfide Catalyst Regulation for Improved Oxygen Evolution Reaction, *Energy Fuels*, 2022, **36**(13), 6675–6694.